Surface reconstruction accuracy using ultrasonic arrays: application to non-destructive testing

Robert E Malkin*[1], Amanda C Franklin[1], Rhodri L T Bevan[1], Hiroshige Kikura[2] & Bruce W Drinkwater[1]

* Corresponding author - Email address: r.e.malkin@gmail.com

Address:

1 - Department of Mechanical Engineering, University of Bristol, Bristol, UK, BS8 1TR

2 - Laboratory for Advanced Nuclear Energy, Tokyo Institute of Technology, Tokyo, Japan

Abstract

The accurate non-destructive inspection of engineering structures using ultrasonic immersion imaging requires a precise representation of the surface of the structure. Here we investigate the relationship between surface geometry, surface measurement error using ultrasonic arrays and the total focusing method (TFM) and how this impacts on the ability to image a feature within a component. Surfaces shaped as sinusoids covering combinations of surface wavelengths (0.8 to $32\lambda_{water}$) and amplitudes (0.6 to $9\lambda_{water}$) are studied. The surface reconstruction errors are shown to cause errors in imaging, such as reduced amplitude and blurring of the image of a side-drilled hole. These reconstruction errors are shown to increase rapidly with the maximum gradient of the sinusoid. Sinusoidal surfaces with maximum gradients $< 45°$ lead to average surface reconstruction errors $< \lambda_{water}$ and amplitude imaging errors within 6dB of the flat-surface case. It is also shown that very poor results are obtained if the surface gradient is excessively steep.

1. Introduction

In ultrasonic non-destructive testing (NDT) an individual transducer, or an array of transducers, are used to insonify the structure under inspection, allowing acoustic energy to propagate into the test structure and then the return echo signals are analysed. When the surface of the structure is uneven two approaches may be utilised; (A) the transducer surface is fitted with a wedge or 'shoe' which has a corresponding negative surface to allow for direct contact [1] or (B) the structure under inspection is placed in a water bath which acts as an acoustic couplant between the transducer and structure surface [2]. The use of shoes has the benefit of being simple to implement, it is however only suited to a single known surface profile and multiple shoes may be needed for even a simple inspection. The immersion approach has the benefit that it can be used for relatively complex surfaces (which need not always be known *a priori*), it is however limited to structures which may be submerged. There also exist a number of 'hybrid' methods which use a conformable coupling material, such as a water-filled bag, between the transducer and the test structure [3], or conformable/flexible arrays which may be placed in direct contact with a curved surface [4–7].

In any ultrasonic technique, the aim is to efficiently transfer acoustic energy from the transducer into the test structure. In order to correctly interpret the return echo signals to form an image of an internal defect the acoustic ray paths must be calculated. For the shoe case this is readily done as

the geometry and materials of both the shoe and the structure surface are known. For the immersion case the ray paths may either be calculated explicitly for a given surface position, for example, using a surface profilometer [6] or determined using the echo data itself [4]. For a surface which is not known *a priori* the echo data can be analysed to determine the location and shape of the structure surface and hence allow accurate imaging of internal features.

To date there is a lack of published literature exploring the influence of the surface geometry on the accuracy of surface reconstructions and internal feature imaging. The recent works of Kerr *et al*. investigated the accuracy of surface reconstructions of 3D metal samples (sphere, cuboid and cylinder) and a more complex human femur bone surface [8,9]. The aim of the present study is to build on such work and elucidate the relationship between an object's surface geometry and the resulting ability to accurately image within it, which is of importance for NDT inspections as a defect's size/severity may be underestimated due to errors in an accurate reconstruction of its surface. This is achieved in two parts, firstly we consider the impact of surface geometry on surface reconstruction accuracy and secondly the resultant impact on internal imaging quality.

Many components in engineering structures consist of curved regions which hamper the use of simple direct-contact inspection, examples include: train wheel axles, nozzle welds and turbine blades. Applying an imaging approach through such surfaces requires the location and geometry of the surface to be known. There are three common methods by which the surface geometry may be measured; (i) the geometry is taken from manufacturing diagrams/photographs or physically measured, (ii) the time of flight between single elements within the array and the surface [10,11], and (iii) the surface geometry can be extracted using an imaging approach such as the Total Focussing Method (TFM) [12,13] or Synthetic Aperture Focusing Technique (SAFT) [8,9,14]. Even minor surface profile errors (less than a fraction of the acoustic wavelength) can result in significant loss of image quality through loss of coherence [15].

Here we use the TFM imaging algorithm [16] and a 1D array to perform 2D imaging. However, we note that the approaches described can equally be applied to other imaging algorithms and extended to 2D arrays and 3D imaging. The TFM algorithm uses all the possible combinations of transmit-receive elements of the array, shown in Figure 1, a data-set set known as Full Matrix Capture (FMC). The TFM algorithm has been shown to have superior resolution compared to traditional imaging algorithms [17] which presents the best resolution for surface reconstruction. It should be noted however that other imaging algorithms (which may have lower spatial resolution) are able to resolve surface geometries with high accuracy [8,9].

For an array of p elements the FMC is generated by firing the first element of the array and recording the echo time domain signal on all p elements. This is repeated for all elements and results in p^2 time domain traces. Figure 1 shows the schematic of the TFM algorithm applied to a material under inspection via a coupling medium. The TFM algorithm is applied post-capture to the FMC data and calculates the image intensity, I, of an arbitrary point, $P(x_2, z_2)$, as given by Eq.1.

$$I(x,z) = \left| \sum h_{T,R}^{Hilb} \left(\frac{d_1}{c_1} + \frac{d_2}{c_2} + \frac{d_3}{c_2} + \frac{d_4}{c_1} \right) \right| \quad (1)$$

Where: $h_{T,R}^{Hilb}$ is the Hilbert transform of the time domain signal from the transmitting element, $T(x_{tx}, z_{tx})$, to the receiving element, $R(x_{rx}, z_{rx})$, $d_{1:4}$ are the ray path distances between $T(x_{tx}, z_{tx})$ the point $P(x_2, z_2)$ and $R(x_{rx}, z_{rx})$, c_1 and c_2 are the longitudinal wave speeds in the coupling medium the material being imaged, respectively. The summation is performed over all possible transmitter-received combinations.

As the longitudinal velocity in the water and the material, c_1 and c_2, are dissimilar the ray paths between array elements and points of interest within the structure need to be calculated. This is achieved by calculating the minimum time-of-flight from $T(x_{tx}, z_{tx})$ to $A(x_1, z_1)$ to $P(x_2, z_2)$ to $B(x_3, z_3)$ to $R(x_{rx}, z_{rx})$ which are the distances $d_{1:4}$ [2,12]. For this calculation the points $A(x_1, z_1)$ and $B(x_3, z_3)$ in Figure 1 need to be found. This is achieved by applying the TFM (or other imaging algorithm) to the whole imaging area and forming a fine image of the interface between the water and the test structure. With the interface measured the minimum time-of-flight between each transmitting and receiving element via each point on the surface is calculated (using Fermat's principle of least time), which in Figure 1 would be distances $d_{1:4}$.

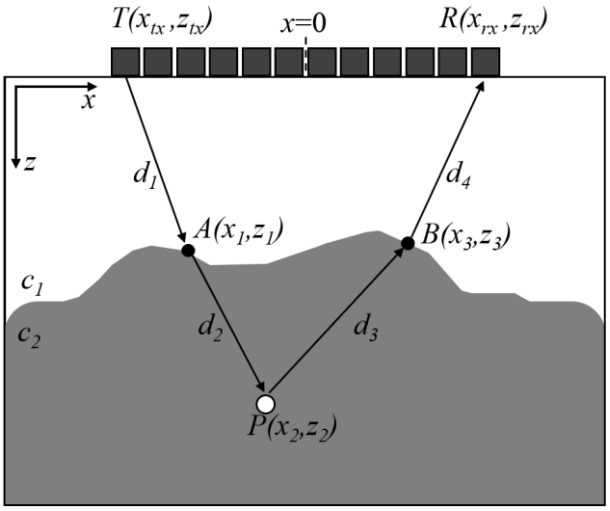

Figure 1 – Application of the TFM algorithm to a test structure in immersion. c_1 & c_2 are the longitudinal wave speed speeds in the immersion fluid (usually water) and the test structure respectively.

2. Test specimens and experimental set-up

To directly address the impact of surface geometry we manufacture a number of sinusoidal-shaped surfaces, the rationale being that arbitrary surfaces may be decomposed into a number of sinusoidal components. As shown in Figure 2a and Table 1, surfaces of $300mm$ in length were formed from $n = 10$ single-cycle sine waves of different wavelengths, ψ_n. Ten amplitude-scaled versions of this surface were then formed to cover a wide range of surface geometries. The amplitude and wavelength of the surfaces are given in terms of the acoustic wavelengths, λ_w, (in water for a central transducer frequency of $5MHz$), in Table 1. At one extreme, this range included relatively flat surfaces where both the amplitude and feature wavelength are < λ_w. At the other extreme highly curved surfaces are included that cause significant image distortion. Each sample also included two flat $5mm$ sections at both ends to act as reference positions. This resulted in 100 single-cycle sine waves with unique combinations of amplitude and wavelength. To study internal imaging a $2mm$ diameter side-drilled hole (SDH) was introduced $10mm$ below each sinusoid, shown in Figure 2b. The surfaces shown in Figure 2 were manufactured by laser cutting 4 layers of $5mm$ thick acrylic ($c = 2730m/s$; density, $\rho = 1180kg/m^3$) and bonded to create $20mm$ thick samples.

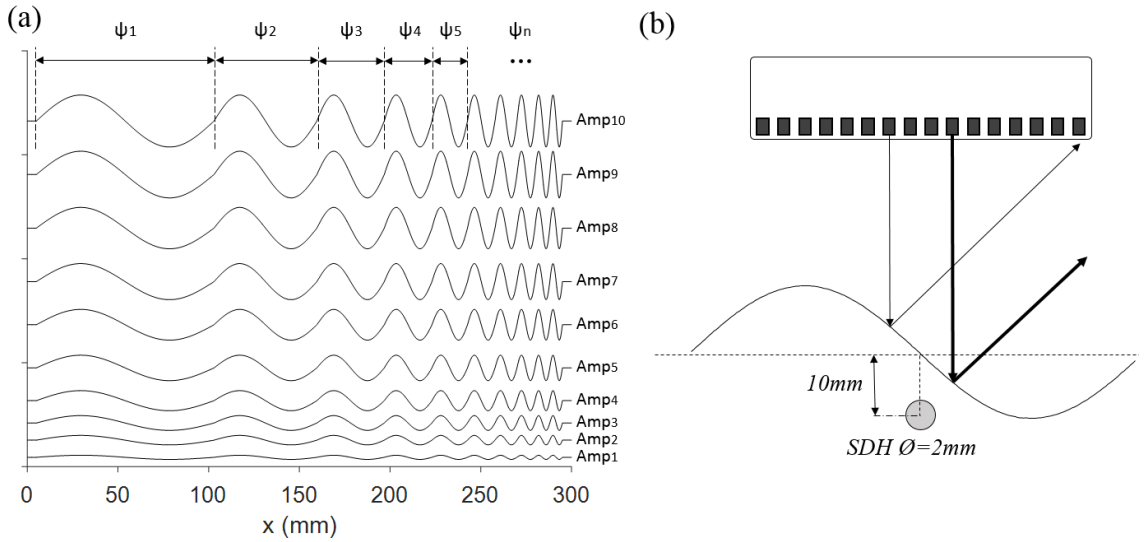

Figure 2 – Test surfaces and feature location. (a) Relative amplitudes ($Amp_{1:10}$) of each of the 10 specimen surfaces ($\psi_{1:10}$). Each surface consists of 10 individual sine waves with lengths (showing the first 5), $\psi_{1:5}$, given in Table 1. (b) The relative location of the SDH for each surface. The horizontal location of the SDH was positioned underneath the steepest section of the sine curve. Normal ray paths reflecting from the surface showing the effect of specular reflection and a finite sized array. The thin reflection path line echo will be received by the array, whereas the thicker echo path line will not be, thus reducing the ability to detect/measure the surface.

Table 1 – Individual sin wave surface parameters and peak-to-peak (PTP) amplitude.

ψ_n	ψ (mm)	λ_w per ψ	Amp_m	Amplitude PTP (mm)	λ_w per Amp
1	108.12	32.00	1	2.00	0.59
2	67.58	20.00	2	5.11	1.51
3	54.06	16.00	3	8.22	2.43
4	21.62	6.40	4	11.33	3.35
5	10.81	3.20	5	14.44	4.27
6	6.76	2.00	6	17.56	5.20
7	5.41	1.60	7	20.67	6.12
8	4.32	1.28	8	23.78	7.04
9	3.60	1.07	9	26.89	7.96
10	2.70	0.80	10	30.00	8.88

The maximum gradient of the surface is use to characterise its severity and is given by,

$$\sigma_{m,n} = tan^{-1}\left(\frac{2\pi\, Amp_m}{\psi_n}\right) \quad (2)$$

where 0° is a flat surface and 90° would be a vertical step. The value of σ for the range of amplitudes ($m = 1{:}10$) and surface lengths ($n = 1{:}10$) featured in the 100 manufactured surfaces is shown in Figure *3*.

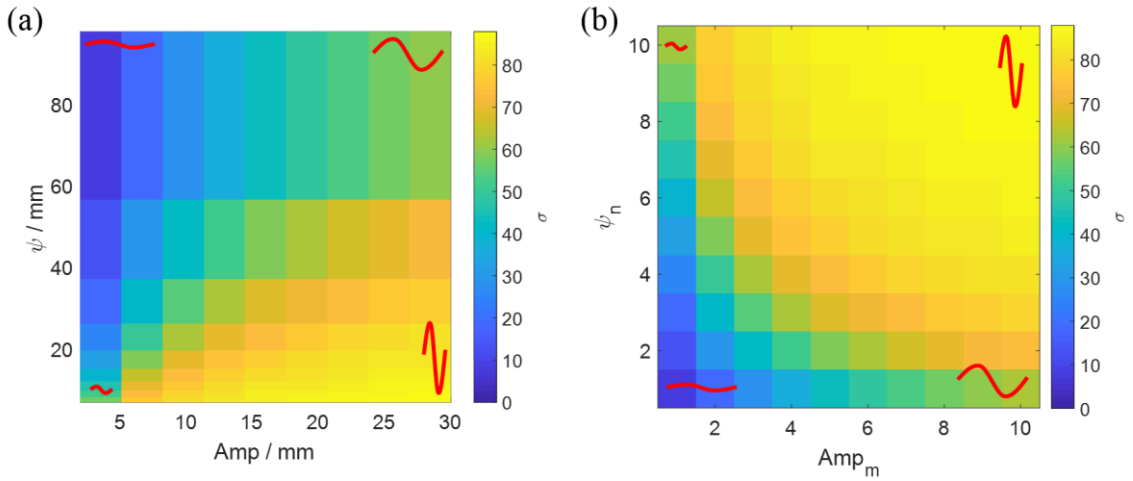

Figure 3 – Maximum surface gradient, σ, for each of the 100 individual surfaces. The data is overlaid with representative individual surfaces in red. The same data is shown in both (a) mm units and (b) the surface wavelength and amplitude number, m,n(1:10) for clarity.

The samples were immersed in a 3-axis computer-controlled scanning system. To image a whole specimen (in length) the array (see table 3 for details) was moved in $10mm$ increments a total of 31 times. Throughout all measurements the probe was held parallel to the z axis. With a known surface geometry it is possible to orientate the array to be parallel to the surface under inspection to maximise transmission of acoustic energy into the sample. Given the array being much larger than many of the spatial features we investigated and making no surface geometry assumptions we kept the array orientation to the sample surfaces fixed. The scanning of the array location and data acquisition was fully automated. At each array location a FMC dataset was captured and a corresponding TFM image created and digitally stored, shown in Figure 4.

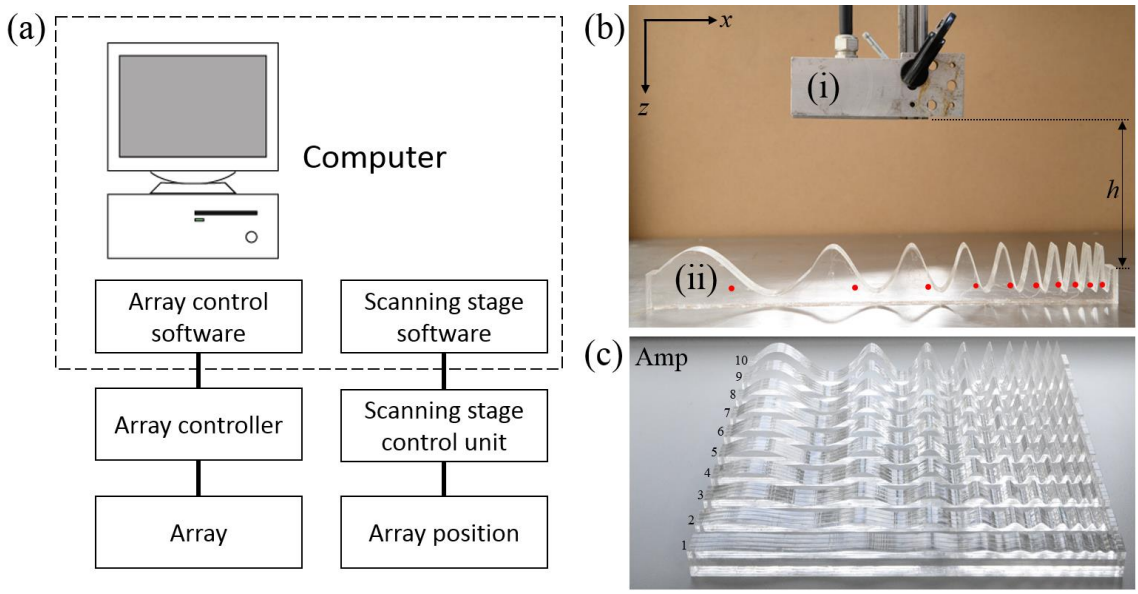

Figure 4 - Data acquisition, scanning system and samples. (a) Data acquisition: The computer controlled both the FMC data acquisition from the array and control of the scanning stage. (b) Scanning system: (i) array and array holder, (ii) sample on scanning stage (shown without water for clarity) and SDH locations highlighted in red for clarity, with stand-off height, h, (c) laser cut samples 1:10.

When applying the TFM algorithm to extract the surface of a sample the ray paths are assumed to be direct and unobstructed. For surfaces with relatively small Amp this is generally true, however for

larger values of Amp and shorter ψ, as shown diagrammatically in Figure 5, the ray paths may be obstructed resulting in path shadowing. We approximate that spatial surface features which will result in shadowing to occur when the ratio of $\frac{\psi}{Amp} < \frac{w}{h}$, where w is the array width. Shadowing will occur for surfaces when $\frac{\psi}{Amp} < \frac{w}{h} = \frac{\psi}{Amp} < 0.56$, where $h = 85mm$. A ratio of 0.56 is the equivalent of the maximum surface inclination angle of $\sigma = 15.6°$.

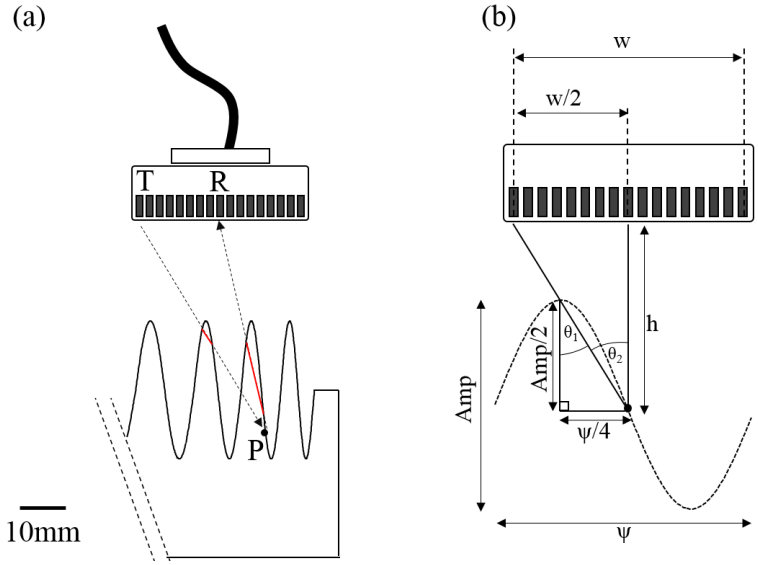

Figure 5 – Shadowing of surfaces features. (a) For certain combinations of Amp and ψ the assumption that ray paths between a given transmitting element, T, a surface point, P, and a receiving element, R, are uninterrupted will no longer hold. The result of this shadowing is to modify the true ray path (shown in red) on both the transmission and reception paths. (b) Our definition of when shadowing occurs. The diagonal line passing through the wave peak and the point of maximum inclination define the point of shadowing.

Table 2 - Array parameters for experimental measurements.

Array parameter	**Value**
Number of elements	128
Element pitch (mm)	0.3
Inter element space (mm)	0.1
Element length (mm)	15
Central frequency (MHz)	5
Bandwidth (-6 dB) (MHz)	3-7

A TFM_{global} image was formed by image stitching; i.e. the process of combining multiple TFM_{local} images with overlapping areas to produce a single TFM_{global} image larger in size than the individual images. To summarise, we used image pixels spaced by $0.1mm$ in both x and z axes and stepped the array in $10mm$ increments along the x axis. As the array was moved in increments less than the array length, some regions of a sample were imaged multiple times, these multiple TFM images were then averaged. Once the TFM_{global} image had been formed the surface profile was extracted to assess the accuracy of surface reconstruction. The first stage in extracting the surface profile was to identify the spatial locations of the first reflected signal above a threshold value (calculated as the median TFM pixel value within the surface region for each TFM_{global} image) for each vertical column of the TFM_{global} image. In an ideal TFM_{global} image each column (a single location in the x direction) would depict part of the measured surface, whereas in reality not all regions are imageable. As the surface reconstruction algorithm was designed to work for any surface type (flat

regions, smooth curves, steps etc) and assumed no prior knowledge of the surface, linear interpolation was deemed suitable. During preliminary testing the use of other interpolation functions yielded no significant difference on measured parameters. The linear interpolation was used to bridge between successfully measured surface points to generate coordinates of the whole surface. Finally, TFM measured surfaces were compared to the true surfaces and the average error, $\Delta_n^{ave.}$ and maximum error, $\Delta_n^{max.}$ for each of the 10 surfaces per sample were calculated using Eq.3 and Eq.4 respectively. Each of these steps is shown in Figure 6 and a close-up view of a sample specimen shown in Figure 7.

$$\Delta_n^{ave.} = \frac{1}{\psi_n}\ \frac{1}{3000}\ \sum_{k=1}^{k=3000} \left| z_{TFM}^k - Z_{true}^k \right| \tag{3}$$

$$\Delta_n^{max} = \ max\left[\left| z_{TFM}^k - Z_{true}^k \right|_{k=1}^{k=3000} \right] \tag{4}$$

Where n is the surface number $(n = 1{:}\,10)$ under study, k is the spatial point number along the x axis of both the TFM extracted surface and the true surface, the total point count was 3000 for the whole length of the sample which corresponds to a spatial sampling of $0.1mm$ which is equal to the pixel spacing used in the TFM algorithm.

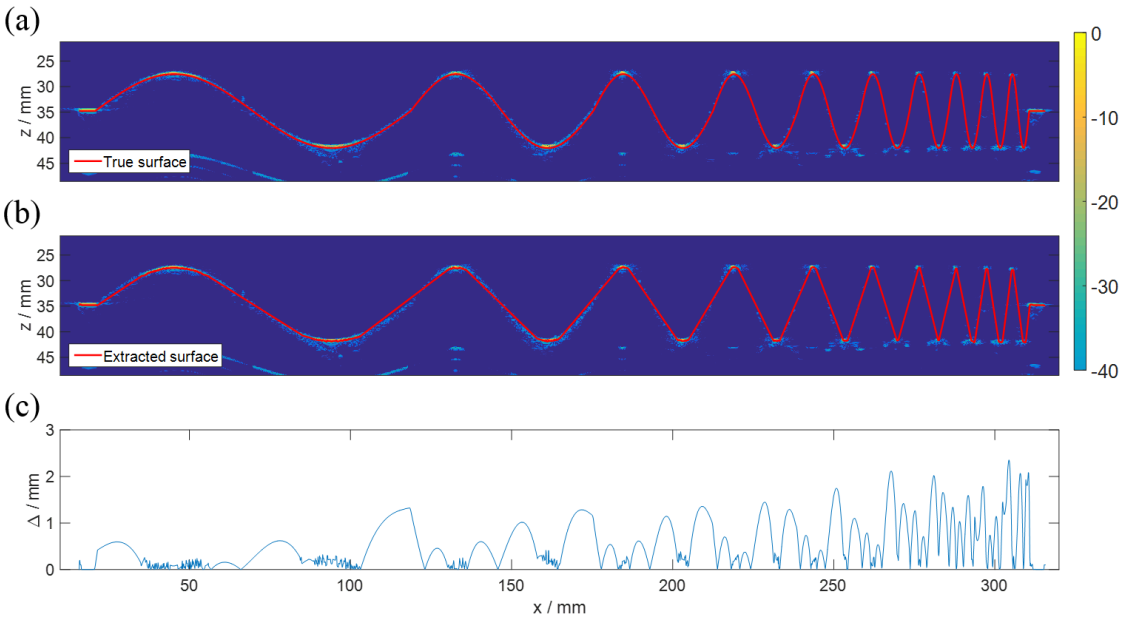

Figure 6 – Surface measurement and error estimation for the Amp_5 sample. (a) Example stitched TFM_{global} image of specimen surface with the true surface superimposed. Note the high amplitude reflection from the peak and trough locations. (b) The stitched TFM_{global} image and the corresponding interpolated surface superimposed. (c) The absolute error between the true and measured surfaces. For a) and b) data normalised to the maximum intensity and plotted on a dB scale.

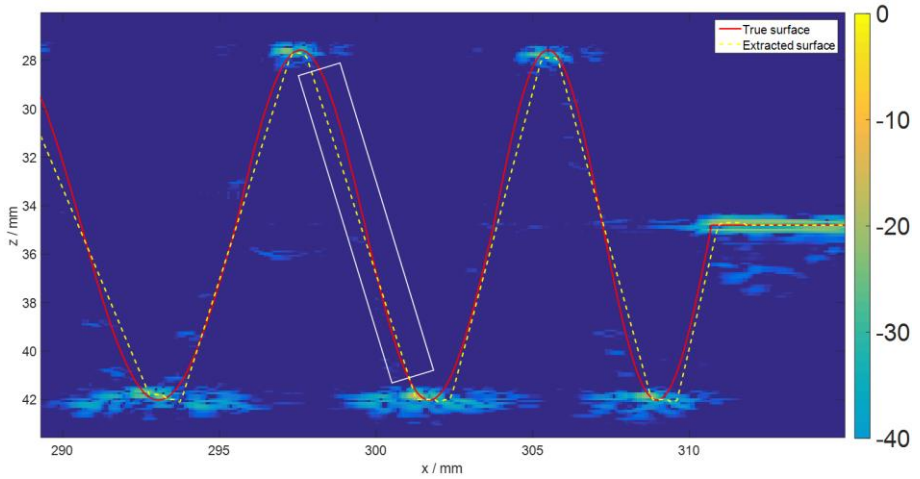

Figure 7 – Close-up view of the example surface ($Amp_5\ \psi_{9:10}$) showing the TFM image, the true surface and the extracted surface. The lack of imagable regions of the surface (representative area shown in the white rectangle) results in errors between the interpolated surface and the true surface. The highly reflective peaks and troughs of each surface give rise to the interpolated triangular representation of the surfaces. The image ($x > 310mm$) shows the flat parts of the samples used as reference points.

3. Surface reconstruction and internal imaging

Figure 8 shows that the reconstruction errors vary monotonically with both Amp and ψ (both average and maximum). Note that the effect stand-off height between the array and the sample on the surface reconstruction was investigated and found to be very minor (in the range $h = 35 - 135mm$, taken from the flat surfaces at the ends of each sample). We therefore show reconstruction errors for a $85mm$ stand-off distance (middle of range tested).

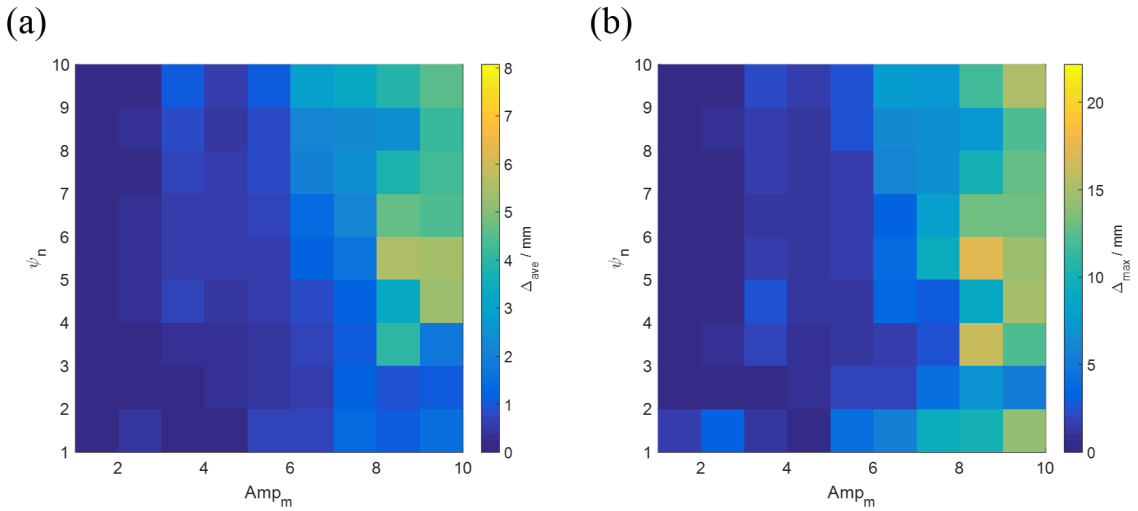

Figure 8 – Surface reconstruction error for a 85mm stand-off height, h. (a) Average error, Δ_{ave} and (b) maximum error, Δ_{max}.

Figure 8 exhibits some high reconstruction errors (around $Amp_m > 8, \psi_n > 5$) which are likely caused by limitations of the surface extraction algorithm where imaging artefacts and/or high amplitude noise pixels in the TFM image may register as points along the surface. The relationship between maximum gradient, σ, and reconstruction errors are shown in Figure 9.

200

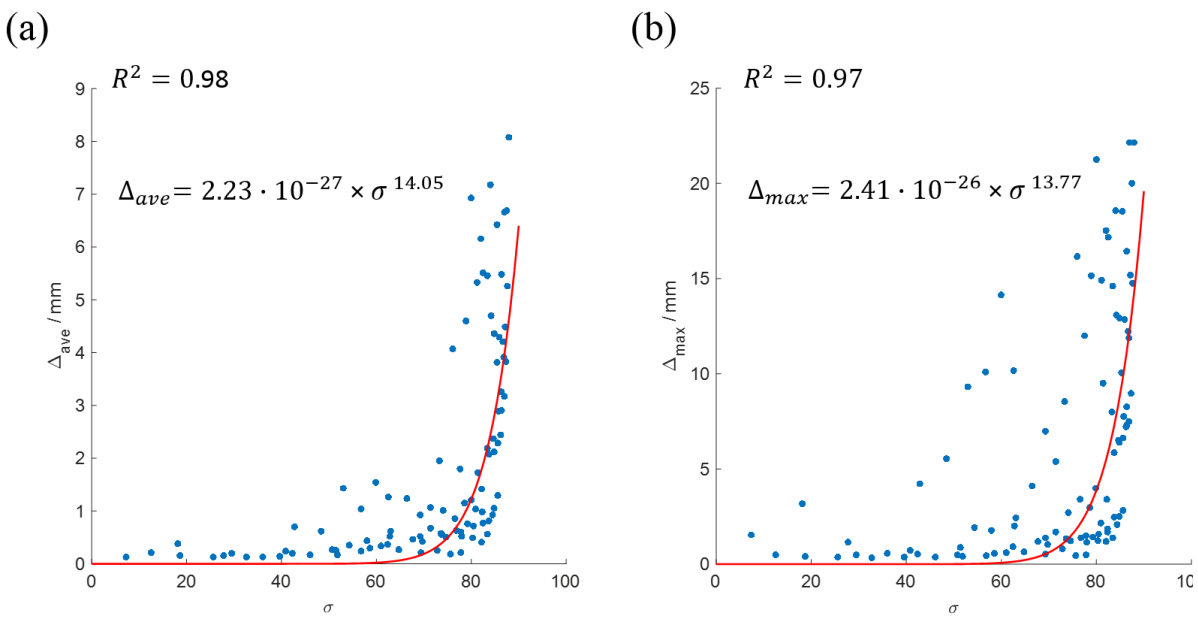

Figure 9 – Correlation between maximum surface gradient and (a) average and (b) maximum errors. Showing coefficient of determination, R^2.

201

202 Figure 9 shows that for $\sigma > 45^{\circ}$ there is a rapid exponential increase in both the average and the
203 maximum reconstruction errors. This suggests that the surface reconstruction algorithm used is
204 unable to accurately extract surface features above this value of σ. With increasing σ the percentage
205 of a surface being accurately measured is reduced resulting in more reliance on the interpolated
206 surface points, as shown in Figure 7. The result being that the true and measured surfaces 'diverge'
207 at $\sigma \approx 45^{\circ}$.

208 Here we investigate how σ impacts on the imaging of internal features. Using the same array (Table
209 2) and surface profiles (reconstructed previously using the experimental TFM_{global} images) we
210 applied adaptive TFM (shown in Figure 1) to image a $2mm$ diameter SDH below each of the sine
211 surfaces ($h = 85mm$). In Figure 10 we show the impact of σ on feature resolution, the
212 corresponding error characterised using the array performance indicator (API) [16], as shown in
213 Eq.5, and the amplitude of the SDH.

$$API = \left(\frac{A_{-6\,dB}}{\lambda^2_{Acrylic}} \right) \tag{5}$$

214

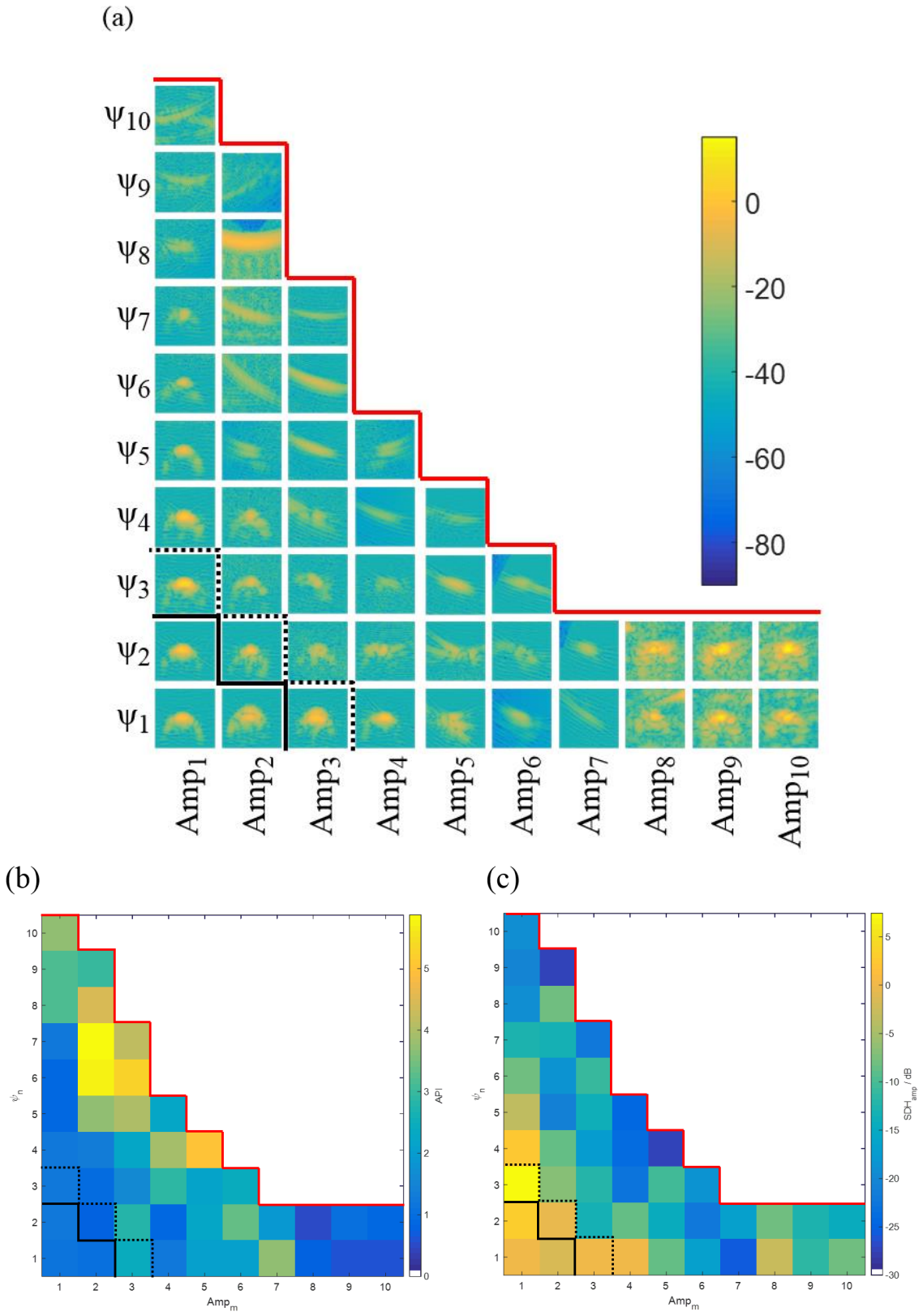

Figure 10 - Influence of surface geometry on API and SDH amplitude. Common lines to all sub plots: red – boundary between SDHs which were regarded as imagable and not, solid black – surface angle at which shadowing begins to occur (only 3 surfaces tested did not exhibit some degree of shadowing), dashed black – surfaces for which σ> critical angle for a planar water- acrylic interface (all but 6 of the tested surfaces featured ray paths with incidence angles greater than the critical angle). (a) SDHs images. Each SDH shown an area 5mm² around the SDH of ø=2mm with dB values scaled to maximum intensity from reference block SDH (b) API for each of the measurable SDHs. (c) SDH_{amp} for each of the SDHs shown in (a).

Where $A_{-6\,dB}$ is the area of the image in which the pixel intensity is greater than $-6dB$ (relative to the peak amplitude of the SDH) and $\lambda_{Acrylic}$ the acoustic wavelength in the acrylic sample. Explicitly, $A_{-6\,dB} = PXL \cdot 0.1^2_{mm}$ where PXL is the number of pixels within $-6dB$ of the peak SDH amplitude and $0.1mm$ is the TFM pixel spacing. We defined a SDH with $API > 10$ to be 'unimagable'. This is a judgement based threshold using the observation that TFM images of SDHs with $APIs > 8$ had no discernible features in the region where the SDH was located. The imagable SHDHs are shown in Figure 10a.

The amplitude of the images of the SDHs were assessed relative to the SDH located below the flat surface of a reference block (same manufacture/materials as above), as shown in Eq.6.

$$SDH_{amp} = 20\log_{10}\left(\frac{I_{SDH}}{I_{SDH}^{ref}}\right) \tag{6}$$

where I_{SDH} is the maximum pixel intensity of the SDH and I_{SDH}^{ref} is the maximum pixel intensity of the SDH below the flat surface.

To quantify the relationship between σ and the API and SDH amplitude we performed regression analysis, shown in Figure 11. SDHs which could not be imaged were removed from the analysis.

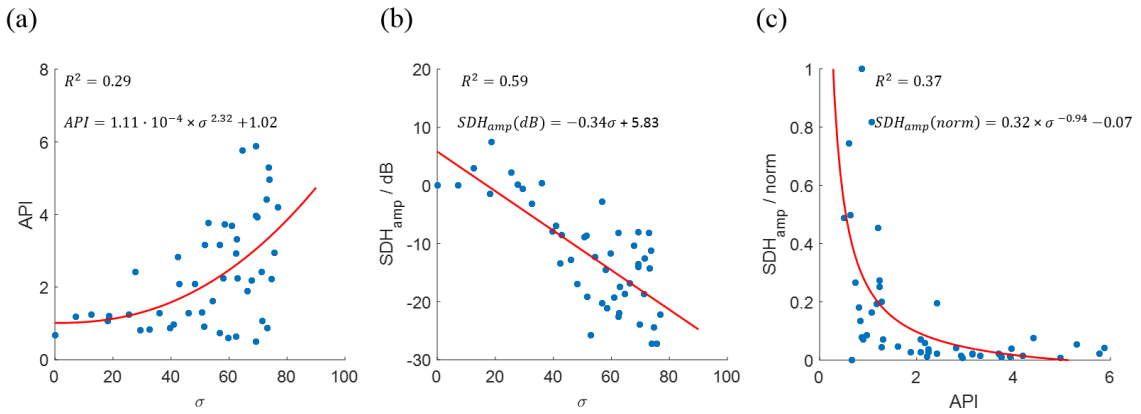

Figure 11 – Influence of σ on both the API and the SDH amplitude, SDH_{amp}. (a) The API is seen to have a scatter but evident dependence on σ. (b) The SDH_{amp} (dB) as a function of σ. (c) SDH_{amp} (normalised) as a function of API, where the SDH amplitude is calculated using Eq.1.

As with the increasing error in surface reconstruction shown in Figure 9 a similar trend is observed in Figure 11a. The increased experimental scatter however precludes a clear indicator at which point the surface gradient results in a large increase in the API. Figure 11b shows that the amplitude of the SDHs drops with increasing surface gradient. Ideal measurements would be insensitive to surface gradient and have no effect on the SDH amplitudes. Figure 11c demonstrates a relationship between the SDH amplitude and the API, which are essentially independent quantities but are determined by σ.

4. Discussion

Spatial shadowing will be more pronounced when an array is closer to the surface, which given that we find a negligible effect on surface reconstruction accuracy would suggest that while shadowing is present for many of our samples, shown in Figure 5, it is a relatively minor effect. The explanation being that even though shadowing is occurring it will only involve a small number of elements at the

extreme ends of the array. This means that shadowing can be thought of as reducing the effective array size.

In addition to shadowing a further effect which may reduce imaging ability is that of the incidence angle. As the surface geometry becomes steeper the incident angle between the surface and the array will increase. Once the water-acrylic critical angle of $32°$ is reached no longitudinal acoustic energy will be transmitted into the material. Imaging is still possible however as the array images the surface over a wide area where the incident angle will be $< 32°$. As per the shadowing effect, the incidence angle is greatest for the extreme end elements and so this effect also acts to reduce the effective array aperture. It is important to highlight that the material properties of the structure under inspection will have a significant effect on the findings presented. Where there is a greater mismatch in the impedances between the couplant and the material two key effects would likely occur: 1) the transmission coefficient into the material would be reduced which would lower the image intensities and 2) the ray path angles within the material would be modified due to increased refraction.

Our study has shown that as σ increases there is a reduction in the accuracy of surface reconstruction and once $\sigma > 45^{\circ}$ there is a rapid increase in the error. Without a sufficiently accurate reconstruction of the surface performing imaging within the material will become less accurate due to loss of spatial and temporal coherence. Additionally once σ is sufficiently high the amplitude of the reflected signal may be too low to be detected because the sound is reflected away from the array position. This effect will be more pronounced with array elements which are highly directional. Therefore, for immersion TFM (or similar) where a sufficiently curved surface needs to be measured, array elements with a wide beam divergence would be preferable. Indeed, such a feature could be included in array optimisation techniques.

When imaging internal features the API and the feature amplitude (in our case SDH_{amp}) are metrics of the imaging quality. The API measures imaging resolution as the spatial extent of a given feature. Given our SDHs were of the same size perfect imaging of the SDHs would give the same API for all SDHs. Figure 11a shows that the API increase with σ, albeit with large scatter. Of particular interest within this scatter are the SDHs corresponding to a large σ and a low API. The likely cause for these counterintuitive results is due to the implementation of the API and its sensitivity to very poorly reconstructed features when the coherent noise becomes comparable to the SDH_{amp}. In effect the API can become directed by noise and its value becomes arbitrary.

The physical meaning of an increasing API is that a feature appears larger in an image which may lead to an over-estimation of feature sizing during an inspection. Similarly, the SDH_{amp} indicates the prominence of a feature in an image where lower SDH_{amp} values suggest a weakly reflecting internal feature. Given our features were all the same size perfect imaging would give us the same SDH_{amp} for all of our SDHs, which is clearly not observed, Figure 11b. It should be noted however that we do not correct for wave amplitude reduction due to the non-planar acoustic ray paths through the acrylic-water interface, which would likely increase SDH_{amp}.

A significant feature of our study is the choice of both the surface type, a sine wave, and the interpolation used. Figure 6a shows an example measured surface where the higher spatial frequencies $200 < x < 300mm$ have been interpolated as triangular wave surfaces. This is due to the peaks and troughs of each of the individual sine waves being parallel to the array thus yielding a high reflection amplitude and therefore being visible whereas the high gradient parts are invisible. The linear interpolation used will then simply connect each of these points with a straight line, creating a triangular surface. The error is therefore the difference between the true surface, a sine

wave, and the measured surface, a triangle wave. As our surfaces were all sinusoidal a spline interpolation function would likely increase the accuracy of the results. As mention previously however the surface reconstruction algorithm was purposefully designed without any prior knowledge of the type of surfaces under inspection.

5. Conclusions

Our work shows the effect of surface geometry on surface reconstruction accuracy and the corresponding quality of imaging a side drilled hole. Our specimens contained 100 single-cycle sine surfaces with varying spatial wavelength and amplitude. As our samples were larger than the array used we developed a method of 'stitching' individual TFM images together into a single global TFM image. The accuracy of reconstruction was quantified by comparing the true surface geometries to the surface geometries interpolated from the global TFM images. The effect of stand-off height was investigated and found to have negligible effect on the accuracy of surface reconstruction.

Our study has shown that as the maximum inclination angle, σ, increases the average and maximum surface measurement errors (across the whole of a single sine wave surface) generally increase. For the imaging of a feature below the interface, in our case a SDH, there is an reduction in imaging accuracy, as measured with the API metric, with increasing surface gradient. This blurring effect is also shown to cause the SDH_{amp} to decrease with surface gradient. Given that all our SDHs were identical, an ideal imaging algorithm would give the same API and SDH_{amp} values for each of the SDHs irrespective of the surface gradient. We have shown that this ideal is only achieved for surfaces with low maximum gradients, i.e. if $\sigma \lessapprox 18^{\circ}$ then the API and SDH_{amp} are within 10% of the flat-surface values. As the surface gradients increase above this level so the API and SDH_{amp} will be 'modified' by the surface through which the inspection is being carried out.

6. Acknowledgements

This work was funded through the UK Engineering and Physical Sciences Research Council (EPSRC) under grant no: EP/N017641/1.

7. References

[1] Drinkwater BW, Bowler AI. Ultrasonic array inspection of the Clifton Suspension Bridge chain-links. Insight - Non-Destructive Test Cond Monit 2009;51:491–8. doi:10.1784/insi.2009.51.9.491.

[2] Zhang J, Drinkwater BW, Wilcox PD. Efficient immersion imaging of components with nonplanar surfaces. IEEE Trans Ultrason Ferroelectr Freq Control 2014;61:1284–95. doi:10.1109/TUFFC.2014.3035.

[3] Long R, Cawley P. Further development of a conformable phased array device for inspection over irregular surfaces. AIP Conf. Proc., vol. 975, AIP; 2008, p. 754–61. doi:10.1063/1.2902738.

[4] Hunter AJ, Drinkwater BW, Wilcox PD. Autofocusing ultrasonic imagery for non-destructive testing and evaluation of specimens with complicated geometries. NDT E Int 2010;43:78–85. doi:10.1016/j.ndteint.2009.09.001.

[5] Lane CJL. The inspection of curved components using flexible ultrasonic arrays and shape sensing fibres. Case Stud Nondestruct Test Eval 2014;1:13–8. doi:10.1016/j.csndt.2014.03.003.

[6] Chatillon S, Cattiaux G, Serre M, Roy O. Ultrasonic non-destructive testing of pieces of complex geometry with a flexible phased array transducer. Ultrasonics 2000;38:131–4. doi:10.1016/S0041-624X(99)00181-X.

[7] Casula O, Poidevin C, Cattiaux G, Dumas P. Control of complex components with Smart Flexible Phased Arrays. Ultrasonics 2006;44:e647–51. doi:10.1016/j.ultras.2006.05.122.

[8] Kerr W, Pierce SG, Rowe P. Investigation of synthetic aperture methods in ultrasound surface imaging using elementary surface types. Ultrasonics 2016;72:165–76. doi:10.1016/j.ultras.2016.08.007.

[9] Kerr W, Rowe P, Pierce SG. Accurate 3D reconstruction of bony surfaces using ultrasonic synthetic aperture techniques for robotic knee arthroplasty. Comput Med Imaging Graph 2017;58:23–32. doi:10.1016/j.compmedimag.2017.03.002.

[10] Camacho J, Cruza JF, Brizuela J, Fritsch C. Automatic dynamic depth focusing for NDT. IEEE Trans Ultrason Ferroelectr Freq Control 2014;61:673–84. doi:10.1109/TUFFC.2014.2955.

[11] Robert S, Casula O, Roy O, Neau G. Real time nondestrutive testing of composite aeronautical structures with a self-adaptive ultrasonic technique. 2012 IEEE Int. Conf. Imaging Syst. Tech. Proc., vol. 24, IEEE; 2012, p. 207–12. doi:10.1109/IST.2012.6295532.

[12] Le Jeune L, Robert S, Dumas P, Membre A, Prada C. Adaptive ultrasonic imaging with the total focusing method for inspection of complex components immersed in water, 2015, p. 1037–46. doi:10.1063/1.4914712.

[13] Robert S, Calmon P, Calvo M, Le Jeune L, Iakovleva E. Surface estimation methods with phased-arrays for adaptive ultrasonic imaging in complex components, 2015, p. 1657–66. doi:10.1063/1.4914787.

[14] Nagai M, Lin S, Fukutomi H. Determination of shape profile by saft for application of phased array technique to complex geometry surface, 2012, p. 849–56. doi:10.1063/1.4716313.

[15] Pinton G, Trahey G, Dahl J. Spatial coherence in human tissue: implications for imaging and measurement. IEEE Trans Ultrason Ferroelectr Freq Control 2014;61:1976–87. doi:10.1109/TUFFC.2014.006362.

[16] Holmes C, Drinkwater BW, Wilcox PD. Post-processing of the full matrix of ultrasonic transmit–receive array data for non-destructive evaluation. NDT E Int 2005;38:701–11. doi:10.1016/j.ndteint.2005.04.002.

[17] Jie Zhang, Drinkwater BW, Wilcox PD. Comparison of ultrasonic array imaging algorithms for nondestructive evaluation. IEEE Trans Ultrason Ferroelectr Freq Control 2013;60:1732–45. doi:10.1109/TUFFC.2013.2754.